

1 Word Count: 8082

2 **Hydrogen incorporation mechanism in the lower-mantle bridgmanite**

3

4 Narangoo Purevjav^{1,2}, Naotaka Tomioka³, Shigeru Yamashita¹, Keiji Shinoda⁴,
5 Sachio Kobayashi³, Kenji Shimizu³, Motoo Ito³, Suyu Fu⁵, Jesse Gu^{5,#}, Christina Hoffmann⁶,
6 Jung-Fu Lin⁵, and Takuo Okuchi^{1,7,*}

7

8 ¹ Institute for Planetary Materials, Okayama University, Misasa 682-0193, Japan.

9 ² Bayerisches Geoinstitut, University of Bayreuth, 95440 Bayreuth, Germany.

10 ³ Kochi Institute for Core Sample Research, X-star, Japan Agency for Marine-Earth Science and
11 Technology (JAMSTEC), Nankoku, Kochi 783-8502, Japan.

12 ⁴ Department of Geosciences, Graduate School of Science, Osaka Metropolitan University.

13 ⁵ Department of Geological Sciences, Jackson School of Geosciences, The University of Texas at
14 Austin, Austin, TX, USA.

15 ⁶ Chemical and Engineering Materials Division, Neutron Sciences Directorate, Oak Ridge
16 National Laboratory, Oak Ridge, TN 37831, USA.

17 ⁷ Institute for Integrated Radiation and Nuclear Science, Kyoto University, Kumatori, Osaka
18 590-0494, Japan.

19 [#]Present address: Department of Earth and Planetary Sciences, Harvard University, Cambridge,
20 MA 02138, USA.

21

22 ***Corresponding author:** okuchi@rri.kyoto-u.ac.jp

23 **Keywords:** bridgmanite, lower mantle, hydrogen substitution, neutron diffraction

24

25

ABSTRACT

26

Bridgmanite, the most abundant mineral in the lower mantle, can play an essential role in deep-

27

Earth hydrogen storage and circulation processes. To better evaluate the hydrogen storage

28

capacity and its substitution mechanism in bridgmanite occurring in nature, we have synthesized

29

high-quality single-crystal bridgmanite with a composition of $(\text{Mg}_{0.88} \text{Fe}^{2+}_{0.05} \text{Fe}^{3+}_{0.05} \text{Al}_{0.03})(\text{Si}_{0.88}$

30

$\text{Al}_{0.11} \text{H}_{0.01})\text{O}_3$ at nearly water-saturated environments relevant to topmost lower mantle pressure

31

and temperature conditions. The crystallographic site position of hydrogen in the synthetic (Fe,

32

Al)-bearing bridgmanite is evaluated by a time-of-flight single-crystal neutron diffraction

33

scheme, together with supporting evidence from polarized infrared spectroscopy. Analysis of the

34

results show that the primary hydrogen site has an OH bond direction nearly parallel to the

35

crystallographic *b* axis of the orthorhombic bridgmanite lattice, where hydrogen is located along

36

the line between two oxygen anions to form a straight geometry of covalent and hydrogen bonds.

37

Our modelled results show that hydrogen is incorporated into the crystal structure via coupled

38

substitution of Al^{3+} and H^+ simultaneously exchanging for Si^{4+} which does not require any cation

39

vacancy. The concentration of hydrogen evaluated by secondary-ion mass spectrometry and

40

neutron diffraction is ~0.1 wt% H_2O and consistent with each other, showing that neutron

41

diffraction can be an alternative quantitative means for the characterizations of trace amounts of

42

hydrogen and its site occupancy in nominally anhydrous minerals.

43

44

45

INTRODUCTION

46 Chemically bonded hydrogen in rock-forming minerals of mafic oceanic lithospheres could
47 survive subduction processes and be transported into the deep Earth via plate tectonic motions
48 (Kawakatsu and Watada 2007; Ohtani et al. 2004; Thompson 1992). The total mass of such
49 hydrogen cycle in the present Earth had been proposed to exceed the mass of surface ocean water
50 (Karato et al. 2020). Crystal structures of hydrous and nominally anhydrous minerals in the deep
51 Earth are possible candidates for transporting such hydrogen into the deep mantle. The hydrogen
52 incorporation in these minerals can involve not only covalent hydroxyl (OH) bonds but also
53 moderate to strong hydrogen bonds as determined primarily by neutron diffraction works
54 (Purevjav et al. 2014; 2016; 2018; 2020; Sano-Furukawa et al. 2011; 2018; Tomioka et al. 2016;
55 Trots et al. 2013; Suzuki et al. 2001). These hydrogen bonds in the host minerals allow hydrogen
56 to stay in the host crystal structures even at relevant high-temperature conditions. Among such
57 hydrogen-hosting minerals, wadsleyite and ringwoodite in the mantle transition zone from 410
58 km to 660 km depth are among the most representative ones and relatively well documented;
59 these minerals can have total water storage capacities as high as six ocean masses (Karato et al.
60 2020 and references therein). The actual existence of hydrogen in the transition zone had also
61 been confirmed by the discovery of a natural hydrous ringwoodite crystal in a diamond inclusion
62 (Pearson et al. 2014).

63 As for the fate of hydrogen beyond 660 km depth, it is essential to consider that some of
64 the oceanic lithospheres can penetrate through the transition zone and carry some hydrogen into
65 the lower mantle (Fukao et al. 2009; Fukao and Obayashi 2013; Portner et al. 2020). The lower
66 mantle, the largest volume fraction of the layered Earth, consists of bridgmanite, ferropericlase,
67 and other minor constituent phases. Bridgmanite likely represents approximately 80 % of the

68 lower-mantle volume (Hirose et al. 2017), such that hydrogen capacity and stability in this
69 mineral phase is one of the primary factors in determining the distribution and circulation of
70 hydrogen within the multi-layered Earth. There have been extensive studies on hydrogen in
71 bridgmanite in past decades, including analyses by Fourier-transform infrared (FTIR)
72 spectroscopy and secondary-ion mass spectrometry (SIMS) for synthetic crystals obtained at
73 relevant high pressure and temperature conditions (Bolfan-Casanova et al. 2003; Litasov et al.
74 2003; Meade et al. 1994; Murakami et al. 2002; Liu et al. 2021; Panero et al. 2015). In addition
75 to these studies, Fu et al. (2019) conducted a combined analysis of polarized FTIR and
76 NanoSIMS to characterize hydrogen in (Fe, Al)-bearing bridgmanite synthesized at nearly water-
77 saturated, uppermost lower mantle conditions. They reported that the single-crystal bridgmanite,
78 $\text{Mg}_{0.88} \text{Fe}^{3+}_{0.065} \text{Fe}^{2+}_{0.035} \text{Al}_{0.14} \text{Si}_{0.90} \text{O}_3$, contains $\sim 1,020(\pm 70)$ ppm of H_2O and displays two
79 pronounced OH^- stretching bands at $\sim 3,230 \text{ cm}^{-1}$ and $\sim 3,460 \text{ cm}^{-1}$. Following these works, here
80 we have focused on the analysis of hydrogen's chemical bonding environments in the crystal
81 structure of (Fe, Al)-bearing bridgmanite. For the first time, the high-quality bridgmanite crystals
82 we synthesized here permit time-of-flight (TOF) Laue neutron diffraction analysis. These results
83 allow us to refine the site of chemically-bonded hydrogen and to model its cation exchange
84 mechanism within the crystal structure. We have also conducted polarized FTIR analysis in all
85 three principal crystal orientations. Together with SIMS analysis of the crystals, these results
86 provide new insights in our understanding of the hydrogen substitution site and mechanism in the
87 crystal structure of bridgmanite.

88

89

CRYSTAL STRUCTURE OF BRIDGMANITE AND ITS HYDROGEN EXCHANGE MECHANISM

90

91 Here we briefly introduce the crystal structure of bridgmanite and its previously proposed
92 hydrogen substitution mechanism as this information will be used to evaluate the actual
93 experimental data for the hydrogen site occupancy in the present study. Figure 1 shows the
94 crystal structure of (Fe, Al)-bearing bridgmanite (space group *Pbnm*), which is the same as that
95 of MgSiO₃ bridgmanite (Horiuchi et al. 1987; Kudoh et al. 1990; Nakatsuka et al. 2021;
96 Sugahara et al. 2006; Ross and Hazen 1989). The A cation site with twelve (or practically eight)
97 oxygen anions (O²⁻) is occupied by either magnesium (Mg²⁺), iron (Fe^{2+/3+}), or aluminum (Al³⁺).
98 The B cation site with six O²⁻ anions is occupied by either silicon (Si⁴⁺) or Al³⁺. There are two
99 O²⁻ sites (O1 and O2), which were proposed to include a minor fraction of vacant sites (V^{••}O)
100 (Navrotsky 1999). Each O1 is shared by two BO₆ octahedra with the bonding direction along the
101 *c*-axis, while each O2 is shared by two BO₆ octahedra with the bonding direction normal to the *c*-
102 axis. Based on the aforementioned crystal structure, two types of hydrogen exchange
103 mechanisms had been proposed for the Al-bearing bridgmanite system. These are (1) Al³⁺ (or
104 possibly Fe³⁺) and H⁺ simultaneously exchange for Si⁴⁺ at a B site (Muir and Brodholt 2018;
105 Townsend et al. 2015), and (2) two Al³⁺ or Fe³⁺ and one V^{••}O simultaneously exchange for two
106 Si⁴⁺ at two B sites, and then some fraction of the generated V^{••}O is coupled with another O²⁻ to
107 simultaneously exchange for two OH⁻ (Litasov et al. 2003; Navrotsky 1999).

108

109 **EXPERIMENTAL AND ANALYTICAL PROCEDURES**

110 **Synthesis**

111 In the previous study, we had synthesized high-quality, inclusion-free crystals of (Fe, Al)-
112 bearing bridgmanite at a fixed pressure-temperature condition of 24 GPa and 1800 °C using a
113 scaled-up Kawai-type cell (Fu et al. 2019; Okuchi et al. 2015). The current synthesis procedure

114 was designed for growing larger crystals several hundreds of μm in sizes while maintaining the
115 quality of the crystals. The starting material was made of a powder mixture of MgSiO_3 ,
116 $\text{Mg}(\text{OH})_2$, ^{57}FeO , and Al_2O_3 , with 64.8, 20.2, 8.9, and 6.1 wt%, respectively. It contains 6 wt% of
117 H_2O , simulating a water-saturated peridotite system. Approximately 15 mg of the mixture was
118 packed into a Pt capsule with outer and inner diameters of 2.3 and 2.0 mm, respectively. The
119 capsule was sealed by welding, inserted into a 14/6 Kawai-type cell assemblage, and then
120 pressurized to 24 GPa by applying a 19 MN load at the Institute for Planetary Materials (IPM),
121 Okayama University. At the targeted pressure, the capsule was heated to 1820 °C and kept for 10
122 minutes to melt the mixture. Then, the temperature was slowly reduced to 1690 °C with a
123 cooling rate of 0.5 °C/min for 4 hours, and even more slowly decreased to 1590 °C with a rate of
124 0.1 °C/min for 12 hours. Finally, the temperature was kept constant for another 4 hours. After
125 this series of temperature control procedures, the sample was quenched by cutting off the power
126 source under high pressure. The assemblage was then decompressed to ambient pressure.

127

128 **Phase identification and major element analysis**

129 After decompression and recovery of the product crystals from the capsule, several crystals
130 were selected and analyzed using micro-focused XRD (Rigaku's RINT RAPID II – CMF) at
131 IPM. The largest dark brownish bridgmanite crystals were $\sim 500 \mu\text{m}$ in size (Fig. 2a). A small
132 fraction of transparent majorite crystals of $\sim 200 \mu\text{m}$ sizes were also found to co-exist with the
133 bridgmanite. Fine-powdered and light-greenish quenched aggregates were also occasionally
134 found, which were identified by XRD analysis as a mixture of dense hydrous magnesium silicate
135 (DHMS) phase D and brucite. This indicates that the bridgmanite crystals were grown in a
136 nearly-water-saturated magmatic environment (Fig. 2b).

137 Major-element compositions of the bridgmanite crystals were determined using a JEOL
138 JXA-8800 electron-probe microanalyzer (EPMA), with operating conditions of 15 kV
139 accelerating voltage, 12.1 nA probe current, and 5 μm probe diameter. Two crystals with
140 polished surfaces were measured by taking four data points from each crystal (Table 1). In
141 addition to these point analyses, macroscopic chemical homogeneity of Mg, Si, Fe, Al, and O
142 within these crystals was confirmed by map analysis. An additional double-side polished crystal
143 $190 \times 170 \mu\text{m}^2$ in size and $\sim 200 \mu\text{m}$ in thickness was prepared for Mössbauer spectroscopy of
144 ^{57}Fe analysis at Advanced Photon Source at the Argonne National Laboratory (Fig. 2c). Ferric
145 iron fraction of the bridgmanite crystal was determined to be $\text{Fe}^{3+}/\Sigma\text{Fe} = \sim 52\%$ (Fig. 2d). Based
146 on these results, the major-element chemical formula of bridgmanite was defined as $\text{Mg}_{0.88}$
147 $\text{Fe}^{2+}_{0.05}\text{Fe}^{3+}_{0.05}\text{Al}_{0.11}\text{Si}_{0.88}\text{O}_3$ including all the cation species except hydrogen.

148

149 **Transmission electron microscopy**

150 Four bridgmanite crystals of 200 – 400 μm sizes were prepared for transmission electron
151 microscopy (TEM) analysis. They were cross-sectioned and polished to prepare for five
152 independent foils of 100 to 150 nm in thicknesses and lateral sizes of $\sim 12 \times \sim 8 \mu\text{m}^2$, using a
153 Hitachi SMI-4050 focused ion beam apparatus. Figure 3 shows representative TEM images of
154 one of the foils using JEOL JEM-ARM200F at the Japan Agency for Marine-Earth Science and
155 Technology (JAMSTEC), which was operated at low magnification TEM mode (Fig. 3a) and
156 high-resolution scanning TEM (HR-STEM) mode (Fig. 3b, c) at 200 kV accelerating voltage.
157 Nano-scale analysis of the samples shows that they are homogeneous and free of inclusions and
158 defects, indicating that hydrogen must be incorporated in the lattice, instead of forming

159 precipitates or inclusions within the crystal. The selected-area electron diffraction patterns also
160 feature sharp spots consistent with a long-range ordered high-quality crystal structure (Fig. 3d).

161

162 **Polarized Infrared and SIMS analysis**

163 Using polarized FTIR spectroscopy, we determined the bonding direction and strength of
164 structural hydroxyls (OH^-) within the three-dimensional lattice of the (Fe, Al)-bearing
165 bridgmanite (Fig. 4). Three crystals of $\sim 400 \mu\text{m}$ sizes were selected for determination of their
166 crystallographic orientations using X-ray precession photography at Osaka Metropolitan
167 University (Fig. 4e and 4f). Double-side polished thin sections of thicknesses from 100 to 350
168 μm were prepared to have orientations normal to the three crystallographic axes of bridgmanite.
169 FTIR spectra of the three sections were taken at IPM using a JASCO FTIR-6200 spectrometer
170 coupled to an IRT-7000 microscope with $10\times$ objective/condenser, a KBr/Ge beamsplitter, an
171 MCT detector, a ceramic infrared light source, and a KRS-5/Al wire-grid polarizer. A series of
172 polarized spectra were collected within each section, where 1,024 scans were accumulated in
173 each spectrum with an aperture size of $50 \times 50 \mu\text{m}$ and a wavenumber resolution of 4 cm^{-1} .
174 Considering the limit of page space, two spectra series from sections normal to a and c axes are
175 shown in detail, which are essential to determine the orientation of the O–H dipoles (Figs. 4a and
176 4b). Nonlinear peak fitting analysis was conducted for these series to model each band. Pole
177 figures were prepared to show the two most important bands within the two spectra series (Figs.
178 4c and 4d). These spectra within each crystal were highly reproducible at several different
179 aperture positions, indicating homogeneous distribution of hydrogen within the crystal.

180 The hydrogen concentration was quantitatively analyzed by SIMS (CAMECA IMS-6F) at
181 JAMSTEC. The other three crystals of $\sim 250 \mu\text{m}$ sizes were embedded in an indium pellet

182 together with standard materials. Sample mounts were ultrasonically washed using acetone and
183 pure water, then dried in a vacuum oven overnight before coating. The mount was then coated
184 with gold of 30 nm thickness, and kept in a SIMS sample chamber in a vacuum for more than a
185 day before the analysis. This procedure worked effectively to reduce background of absorbed
186 water on the sample surface. In the SIMS measurements, a primary $^{133}\text{Cs}^+$ beam operated at 1 nA
187 and 14.5 keV was focused to a 15 μm spot on the sample surface. Normal incident electron
188 shower was used for electrostatic charge neutralization of the sputtering area. A field aperture
189 was used to permit transmission of ions from the central area of 10 μm in diameter of the
190 sputtered region to minimize the hydrogen signals from remaining absorbed water on the sample
191 surface. The secondary ions of ^1H , ^{12}C , and ^{30}Si were collected from the sputtered area
192 sequentially by an electron multiplier with 1 second \times 20 cycles. Total duration of each analysis
193 was \sim 5 minutes, including 120 seconds of pre-sputtering. For hydrogen standard materials, we
194 used (i) natural amphibole from the Ichinome-gata volcano (Miyagi and Yurimoto 1995) and (ii)
195 aphyric glass of a mid-oceanic ridge basalt EPR-G3 from the East Pacific Rise (Shimizu et al.
196 2017), which were reported to contain 1.66 and 0.22 wt% of H_2O , respectively (Fig. 5). As for
197 the dry silicate standard for background analyses of hydrogen and carbon, San Carlos olivine
198 was used. While we measured ^{12}C for monitoring contaminations from invisible scratches or
199 cracks on the minerals, we did not observe any irregularly-higher $^{12}\text{C}/^{30}\text{Si}$ ratios than the carbon
200 background. In order to determine the hydrogen concentration in sample crystals, five to seven
201 data points were collected from different portions of each crystal, where we once again
202 confirmed that hydrogen was homogeneously distributed within these crystals, as in the case of
203 FTIR results. Figure 5 shows our procedure to determine the hydrogen concentration as H_2O in
204 the samples assuming a linear relationship between their concentrations and the $^1\text{H}/^{30}\text{Si}$ ratio. We

205 did not conduct background correction of H₂O because the observed ¹H/³⁰Si ratio of San Carlos
206 olivine was negligibly small compared with the sample crystals. The H₂O concentration in the
207 bridgmanite was either 630(40) or 810(50) ppm: the former was obtained using the natural
208 amphibole standard and the latter was obtained using the EPR-G3 glass, respectively. These
209 results are compared with the neutron diffraction results that are described later in this paper.

210

211 **Neutron diffraction and major element distribution**

212 As collaboratively demonstrated by the datasets of EPMA, HR-(S)TEM, FTIR, and SIMS
213 analyses, the synthesized (Fe, Al)-bearing bridgmanite crystals were chemically homogeneous in
214 their major cations and hydrogen distributions (Okuchi et al. 2015). In the present study, we aim
215 to refine the site position of hydrogen in the bridgmanite crystal structure, where neutron
216 diffraction plays the most essential role. To achieve the task, it is essential to find site
217 distributions and occupancies of all major cations and anions in addition to hydrogen, because
218 hydrogen can only become visible after removing all scattering densities of these stronger
219 neutron scatters from the bridgmanite lattice space. One of the largest crystals was selected for
220 neutron diffraction, which was 0.4 × 0.5 × 0.15 mm³. The crystal was exposed to the neutron
221 beam for ~2.5 days in total at a TOF Laue diffractometer TOPAZ installed at the Spallation
222 Neutron Source (SNS), Oak Ridge National Laboratory, which was operated at 1.4 MW proton
223 beam power (Schultz et al. 2014). The crystal was cooled down to 100 K by cold nitrogen gas,
224 where the signal-to-noise ratio of higher-order reflections was enhanced (Purevjav et al. 2016,
225 2018, 2020). For covering the full reciprocal space, we sequentially reoriented the crystal to have
226 25 different orientations with the help of the CrystalPlan software (Zikovskiy et al. 2011). The
227 obtained *hkl*-intensity dataset was refined using the General Structure Analysis Software (Larson

228 and Von Dreele 2004). The optimized structure parameters are summarized in Table 2. The
229 refined space group of the bridgmanite crystal is *Pbnm*, consistent with the previous studies. The
230 lattice constants determined at 100 K are $a = 4.8071(2)$ Å, $b = 4.9473(1)$ Å, and $c = 6.9141(2)$ Å.

231 Based on the EPMA analysis, we have obtained the total occupancies of A and B sites for
232 Mg, Fe, Al, and Si cations. Upon defining their relative distributions between A and B sites (Fig.
233 1), we considered their preferences reported in the previous crystal-chemical studies of
234 aluminous and/or ferrous bridgmanite: (i) Mg and Fe strongly prefer the A site, (ii) Si strongly
235 prefers the B site, and (iii) Al moderately prefers the B site, which are all due to the relations
236 between the relevant site volumes and ionic radii (Lin et al. 2016; Nakatsuka et al. 2021; Nishio-
237 Hamane et al. 2005). In addition, Al can be distributed into the A site when the capacity of the B
238 site is exceeded, as confirmed by the stability of the bridgmanite structure along the solid
239 solution of MgSiO_3 and $\text{Mg}_3\text{Al}_2\text{Si}_3\text{O}_{12}$ (Hirose et al. 2001; Kubo and Akaogi 2000). Therefore,
240 in our structural refinements, Mg and Fe were all fixed in the A site and Si was fixed in the B site,
241 whereas Al occupancies were refined between the A and B sites while constraining their total to
242 be equal with the bulk analytical result from EPMA. As shown in Table 2, this constrained
243 refinement procedure for cation occupancies provided a very reasonable solution: the neutron
244 coherent scattering length of ^{57}Fe (=2.3), Al (=3.45), Si (=4.15), and Mg (=5.38) are all
245 substantially different from each other, guaranteeing that their site distribution was solidly
246 constrained as long as the scattering intensity dataset had enough quality. We found that the total
247 occupancy of the A site was 1.01 as the sum of Mg, Fe, and Al nuclear site occupancies, where
248 its total cation charge was 2.11 as the sum of Mg^{2+} , Fe^{2+} , Fe^{2+} , and Al^{3+} valences. We also found
249 that the total occupancy of the B site was 0.99 as the sum of Al and Si nuclear site occupancies,
250 where its total cation charge was 3.84 as the sum of Al^{3+} and Si^{4+} valences. The total cation

251 valence charge at the A and B sites was $2.11 + 3.84 = 5.95$, which was smaller than the total
252 anion charge of 6.00, as necessarily expected when hydrogen cations were additionally involved
253 within the crystal structure. From these results on the nuclear site occupancies, we concluded that
254 Fe^{2+} or Fe^{3+} did not substantially exist in the B site, which was in contrast to some previous
255 reports (Frost and Langenhorst 2002; Hummer and Fei 2012; Litasov et al. 2003). We note that
256 the results were obtained along with the refined scale factor that assured full occupancies of the
257 two oxygen sites (Table 2). Unreasonable cation site deficiencies in both the A and B sites would
258 be necessary if we instead assumed nontrivial oxygen site vacancies, as previously proposed
259 (Navrotsky 1999).

260

261 **Neutron diffraction and hydrogen site analysis**

262 Normal hydrogen (^1H) generates negative scattering length density distribution of neutrons,
263 whereas all other atoms generate positive densities. Therefore, even if the concentration of
264 hydrogen is much smaller than the other atoms, its position can still be detectable as a unique
265 negative anomaly in the three-dimensional scattering density map (Fourier map). To find such an
266 anomaly in our data, we obtained a difference-Fourier map similar to the case of our previous
267 work (Purevjav et al. 2018). We calculated this map using the difference between all major
268 cation and anion densities and the observed neutron scattering densities. In order to discriminate
269 the hydrogen site, we refined the coordinates, the occupancy, and the Debye-Waller factors of
270 each candidate position step-by-step as suggested from each apparently negative anomaly in the
271 difference map. These procedures in finding the candidate site were made for sixty-three
272 candidate positions located at distances of 0.7 Å to 1.3 Å measured from the nearest oxygen site.
273 As explained later in the discussion, only one of them, shown in Figure 6, was fully consistent

274 with the other analytical results, such that we defined it as the primary hydrogen site shown in
275 Table 2.

276

277 **Neutron diffraction and hydrogen concentration**

278 After finding the primary site, we try to evaluate its occupancy which is equivalent to the
279 hydrogen concentration in the crystal structure. This is a much more challenging task than
280 finding the site, because of its small occupancy, low site symmetry, and very large Debye-Waller
281 factors, all consistently make the quantitative evaluation of scattering density of hydrogen
282 difficult. We previously reported that the accuracy of refined hydrogen occupancy is secured by
283 its stability as a function of resolution in space, where the resolution increases with increasing
284 number of reflections at smaller *d*-spacings (Purevjav et al. 2016; 2018). Following this
285 methodology, we evaluated the hydrogen occupancy in bridgmanite (Fig. 7). It was proved to be
286 stable throughout the whole resolution range to provide best-effort site occupancy of
287 0.010 ± 0.003 (Table 2).

288

289 **RESULTS AND DISCUSSION**

290 **Primary site position deduced from infrared and neutron results**

291 Using the polarized FTIR results, here we discuss the most-plausible hydroxyl bonding
292 strength and direction in the bridgmanite. It was suggested that multiple bonding geometries
293 coexisted within the crystal structure, because of such broad and orientation-dependent infrared
294 absorption profiles, which ranged from 2300 cm^{-1} to 3800 cm^{-1} (Fig. 4). The bonding geometries
295 must also be highly anisotropic within the bridgmanite structure. By carefully evaluating the
296 orientational dependence of the profiles, we assigned four coexisting vibration bands, which

297 have peak wavenumbers at $3480(\pm 40) \text{ cm}^{-1}$, $3160(\pm 20) \text{ cm}^{-1}$, $2880(\pm 20) \text{ cm}^{-1}$, and $2680(\pm 50) \text{ cm}^{-1}$,
298 respectively. The integrated area intensity of the 3160 cm^{-1} band was much more significant
299 than the 3480 cm^{-1} band (Figs. 4c and 4d) and also than the other two. Therefore, even
300 considering the negative correlation between the molar absorption coefficient and the OH
301 stretching wavenumber (Libowitzky and Rossman, 1997), the most intense 3160 cm^{-1} band still
302 showed the property of the most important hydrogen site. The next strongest 3480 cm^{-1} band
303 showed the property of the second site. When the section normal to the a axis was analyzed (Fig.
304 4c), these two bands had common strong pleochroism with the largest absorbances along the b
305 axis and very small absorbances along the c axis. Therefore both of these OH dipoles were
306 oriented normal to the c axis. When the section normal to the c axis was analyzed (Fig. 4d), the
307 two bands showed reversing moderate pleochroism. While the 3160 cm^{-1} band showed the
308 largest absorbance around the b axis, the 3480 cm^{-1} band showed the largest absorbance around
309 the a axis. Their wavenumbers were reported to quantitatively reflect hydrogen bonding strength;
310 it is reasonable to assume that the 3160 cm^{-1} band was from hydroxyls with a moderately-strong
311 hydrogen bond, while the 3480 cm^{-1} band was from that with a very weak hydrogen bond
312 (Libowitzky 1999). While the crystal orientation information was less clarified than in the
313 current case, the coexistences of these two bands and their coherent behavior against crystal
314 orientation were already observed by infrared analysis of (Fe, Al)-bearing bridgmanite (Fu et al.
315 2019; Litasov et al. 2003). Considering the features of the two strong bands, we conclude that the
316 most important hydrogen site formed hydroxyls approximately aligned along the b axis with
317 moderately-strong hydrogen bonding, whereas the second site approximately aligned along the a
318 axis with very weak hydrogen bonding.

319 With the new insights from these infrared results, it follows that the primary hydrogen site is
320 located between two O1 oxygen anions, which is the most-consistent solution among the
321 possible candidates suggested from the neutron diffraction results. These two O1 oxygens form
322 an edge of the A site dodecahedron, where the hydrogen is installed with a hydrogen bonding
323 angle of $179(6)^\circ$ (Fig. 6), forming a straight bonding geometry along the edge. The covalent
324 hydroxyl bond has a distance of $1.03(7)$ Å and the counterpart hydrogen bond has a distance of
325 $1.81(7)$ Å. The hydrogen sites related to the other three bands at 3480, 2880, and at 2680 cm^{-1} are
326 not yet clearly resolved by neutron diffraction. Nonetheless, they show substantial pleochroism
327 as a function of orientation, making them definable as independent bands. We currently do not
328 have any conclusive solution on their crystallographic geometry. A suggestion may come from
329 previous infrared evidence for another nominally anhydrous mineral having an octahedrally-
330 coordinated Si cation site. For example, a remarkably-similar infrared band of very weak
331 absorption at $2659\text{--}2667\text{ cm}^{-1}$ was reported for both Al-free and Al-bearing stishovite, where
332 either reaction of $\text{Si}^{4+} \leftrightarrow \text{Al}^{3+} + \text{H}^+$ or $\text{Si}^{4+} \leftrightarrow 4\text{H}^+$ was proposed to generate its wide variety of
333 hydroxyl absorption bands (Litasov et al. 2007). In addition, a combination of two broad but
334 distinct bands at around 2900 cm^{-1} and 2650 cm^{-1} were reported to exist in Al-free stishovite
335 experiencing $\text{Si}^{4+} \leftrightarrow 4\text{H}^+$ hydration reaction (Spektor et al. 2016). Thus, the bands at the lower
336 wavenumbers observed in bridgmanite could come from clustered hydrogen around the vacant B
337 site, although further studies are necessary to clarify the nature of such hydrogen clusters in the
338 crystal structure of bridgmanite.

339

340 **Hydrogen substitution mechanism**

341 In previous works using neutron diffraction, we successfully determined full structure
342 parameters of several dense hydrogen-bearing minerals occurring in the mantle transition zone,
343 including both nominally hydrous and anhydrous types (Purevjav et al. 2014; 2016; 2018; 2020).
344 It has been demonstrated that octahedrally coordinated Mg^{2+} or Fe^{2+} , as well as tetrahedrally
345 coordinated Si^{4+} , were removed to exchange for hydrogen. That is, hydrogen clusters are
346 generated around the sites originally filled by Mg^{2+} , Fe^{2+} , and Si^{4+} cations. On the other hand, in
347 the bridgmanite structure in the lower mantle, these major cations remain even after the
348 hydration reaction. In other words, it is preferred to avoid creating any cation vacancy as well as
349 hydrogen clusters. By simply referring to the total cation occupancy of 1.01 and its valence
350 charge of 2.06 in the A site, it is clear that hydrogen clustering around such a fully filled site with
351 such an excess charge is energetically unfavorable. We thus conclude that one hydrogen around
352 one filled cation is the unique solution most consistent with the neutron diffraction result (Fig. 6
353 and Table 2). On the other hand, the total cation charge of 3.94 in the B site must be
354 compensated by such an addition of hydrogen around oxygen anions surrounding the site. Since
355 Al^{3+} causes the smaller charge in the B site, the major hydrogen exchange reaction in (Fe, Al)-
356 bearing bridgmanite must be (1') Al^{3+} and H^+ simultaneously exchanging for Si^{4+} in the B site
357 (Muir and Brodholt 2018; Townsend et al. 2016). We note that the addition of hydrogen only
358 increases the total cation charge to 5.96, which is still smaller than the total anion charge of 6.00.
359 The origin of the remaining difference (0.04 per formulation) is still not clear; it is not reasonable
360 to assume a far larger concentration of hydrogen in this site, as explained later. While we may
361 ascribe some fraction of this difference by possible uncertainty of EPMA analysis and
362 Mössbauer results, further research is necessary to solve this issue on the missing cation valence
363 charge.

364

365 **Hydrogen concentration**

366 To provide a reliable hydrogen concentration in aluminous bridgmanite which has been
367 greatly debated so far (Fu et al. 2019; Litasov et al. 2003; Liu et al. 2021; Murakami et al. 2002),
368 and also to evaluate the technical limit of single-crystal neutron diffraction for a trace amount of
369 hydrogen, we finally compare and discuss the concentration values obtained by neutron
370 diffraction and SIMS schemes to each other. Our SIMS results show that the H₂O concentration
371 is between 630(±40) and 810(±50) ppm (Fig. 5). On the other hand, our neutron diffraction
372 results show that the hydrogen site occupancy is 0.010(±0.003) which corresponds to its bulk
373 concentration of 870(±260) ppm (Fig. 7). These results are rather consistent with each other,
374 suggesting that single-crystal neutron diffraction can be an alternative means for a quantitative
375 evaluation of hydrogen concentration as low as 900 ppm = 0.09 wt% of H₂O. We also note that
376 our infrared results suggest the existence of minor hydrogen site(s) which were not revealed in
377 the analysis of neutron diffraction data, but could still be detected in the SIMS analysis results.
378 Further neutron diffraction research using even larger crystals with significantly larger volumes
379 could be useful to address other remaining questions in hydrated bridgmanite.

380

381 **IMPLICATIONS AND CONCLUSIONS**

382 In this study, we have determined the full crystallographic parameters of hydrous (Fe, Al)-
383 bearing bridgmanite, including its hydrogen site position and occupancy, using the TOF Laue
384 neutron diffraction scheme. The diffraction experiments were proved successful due to the use of
385 large and high-quality bridgmanite crystal synthetically grown in a nearly water-saturated
386 environment. Together with the complementary dataset of polarized infrared spectroscopy, our

387 results show that both the hydroxyl covalent bond and the hydrogen bond are directed nearly
388 parallel to the crystallographic *b* axis. The water concentration in bridgmanite has been
389 quantitatively evaluated by SIMS analysis, in addition to the neutron diffraction scheme. These
390 results for water concentration are self-consistent and complementary to each other, showing that
391 neutron diffraction can be used to detect its trace amount as low as ~0.1 wt% H₂O.

392 It was demonstrated that hydrogen is incorporated into the bridgmanite crystal structure via
393 the coupled exchange reaction of H⁺ and Al³⁺ for Si⁴⁺ (H⁺ + Al³⁺ ↔ Si⁴⁺), which does not require
394 the presence of a cation vacancy. That is, hydration in bridgmanite is not accompanied with the
395 creation of any vacancies or any hydrogen clusters, which is in marked contrast to the previously
396 reported hydrogen substitution mechanisms in hydrous minerals in the upper mantle, such as
397 wadsleyite, ringwoodite, and DHMS phase E (Purevjav et al. 2014; 2016; 2018; 2020; Sano-
398 Furukawa et al. 2011; Tomioka et al. 2016). We consider that this contrast is due to the densely-
399 packed nature of the bridgmanite structure, where larger numbers of oxygen anions coordinate
400 single cation. Therefore, it is energetically unfavorable to remove such a cation to create a
401 vacancy while keeping the structure. Multiple hydrogen occupancy within one vacant site
402 (Purevjav et al. 2014; 2016) or creation of hydrogen clusters (Purevjav et al. 2018) are prohibited
403 in the structure of bridgmanite without vacancies, implying that its hydrogen concentration is
404 much more limited than the upper mantle minerals which can have numerous cation vacancies.
405 We thus reinforce the prevailing concept that the upper mantle, including the transition zone,
406 keeps more water than the lower mantle (Karato et al, 2020). In addition, the absence of cation
407 vacancy in hydrous bridgmanite in the lower mantle is important for considering its rheological
408 behavior. We confirmed the result of Muir and Brodholt (2018) by first principle calculation,

409 where hydration of bridgmanite cannot promote hydrolytic weakening because the prevailing
410 $\text{Al}^{3+} + \text{H}^+$ coupling mechanism does not create any cation vacancies.

411 It had been previously proposed that the geometry of chemical bonding around hydrogen
412 atoms in the hydrogen-bearing deep-mantle minerals are determined with high accuracy by using
413 smaller *d*-spacings in the TOF single-crystal experiments (Okuchi et al., 2015). Our study here
414 demonstrates that the distances of covalent and hydrogen bonding and the angle between them
415 can be measured even for the trace amount of hydrogen in the bridgmanite single crystal. This
416 result opens a new window of research opportunity to analyze hydrogen positions and
417 concentrations in other deep-mantle nominally anhydrous minerals by making full use of such
418 neutron diffraction instruments. This type of future studies can help to understand the hydrogen
419 substitution mechanism and water solubility in wide variety of minerals in the deep Earth.

420

421 **ACKNOWLEDGEMENTS AND FUNDING**

422 We acknowledge E. Ito at IPM for technical suggestions in high-pressure synthesis, Y.
423 Yachi at IPM for supporting EPMA analysis, I. Miyagi at National Institute of Advanced
424 Industrial Science and Technology for providing natural amphibole standard for SIMS, X. Wang
425 at SNS for supporting neutron data analysis, and Wenli Bi and Ercan Alp at Argonne National
426 Laboratory for Mössbauer analysis. This work was supported by the Japan Society for the
427 Promotion of Science (Post-doctoral Fellowship for Research in Japan Grant Number P17331,
428 and KAKENHI Grant Numbers 17H01172 and 21H04519). J.F.L. acknowledges support from
429 the Geophysics Program and the Cooperative Studies of The Earth's Deep Interior Program
430 (CSEDI) of the National Science Foundation (EAR-2001381; EAR-1916941). A portion of this
431 research at the Spallation Neutron Source was sponsored by the Scientific User Facilities

432 Division, Office of Basic Energy Sciences, U.S. Department of Energy. This work was supported
433 in part by the Joint Use Program at IPM, by the Kochi Core Center Open Facility System
434 (KOFS) under the MEXT foundation, and by the collaboration research project of Integrated
435 Radiation and Nuclear Science, Kyoto University (R3148, R4011 and R5007).

436

437

REFERENCES CITED

438 Bolfan-Casanova, N., Keppler, H., and Rubie, D.C. (2003) Water partitioning at 660 km depth
439 and evidence for very low water solubility in magnesium silicate perovskite. *Geophysical*
440 *Research Letters*, 30, doi:10.1029/2003GL017182.

441 Frost, D.J., and Langenhorst, F. (2002) The effect of Al₂O₃ on Fe-Mg partitioning between
442 magnesiowüstite and magnesium silicate perovskite. *Earth and Planetary Science Letters*,
443 199, 227–241.

444 Fu, S., Yang, J., Karato, S.i., Vasiliev, A., Presniakov, M.Y., Gavriiliuk, A.G., Ivanova, A.G.,
445 Hauri, E.H., Okuchi, T., Purevjav, N., and Lin, J.F. (2019) Water concentration in single-
446 crystal (Al,Fe)-bearing bridgmanite grown from the hydrous melt: Implications for
447 dehydration melting at the topmost lower mantle. *Geophysical Research Letters*, 46, 10346–
448 10357.

449 Fukao, Y., and Obayashi, M. (2013) Subducted slabs stagnant above, penetrating through, and
450 trapped below the 660 km discontinuity. *Journal of Geophysical Research: Solid Earth*, 118,
451 5920–5938.

452 Fukao, Y., Obayashi, M., and Nakakuki, T. (2009) Stagnant slab: A review. *Annual Review of*
453 *Earth and Planetary Sciences*, 37, 19–46.

- 454 Hirose, K., Fei, Y., Ono, S., Yagi, T., and Funakoshi, K. (2001) In situ measurements of the
455 phase transition boundary in $\text{Mg}_3\text{Al}_2\text{Si}_3\text{O}_{12}$: implications for the nature of the seismic
456 discontinuities in the Earth's mantle. *Earth and Planetary Science Letters*, 184, 567–573.
- 457 Hirose, K., Sinmyo, R., and Hernlund, J. (2017) Perovskite in Earth's deep interior. *Science*, 358,
458 734–738
- 459 Horiuchi, H., Ito, E., and Weidner, D. (1987) Perovskite-type MgSiO_3 : Single-crystal X-ray
460 diffraction study. *American Mineralogist*, 72, 357–360.
- 461 Hummer, D.R., and Fei, Y. (2012) Synthesis and crystal chemistry of Fe^{3+} -bearing
462 $(\text{Mg,Fe}^{3+})(\text{Si,Fe}^{3+})\text{O}_3$ perovskite. *American Mineralogist*, 97, 1915–1921.
- 463 Karato, S., Karki, B., and Park, J. (2020) Deep mantle melting, global water circulation and its
464 implications for the stability of the ocean mass. *Progress in Earth and Planetary Science*, 7,
465 76.
- 466 Kawakatsu, H., and Watada, S. (2007) Seismic evidence for deep-water transportation in the
467 mantle. *Science*, 316, 1468–1471.
- 468 Kubo, A., and Akaogi, M. (2000) Post-garnet transitions in the system $\text{Mg}_4\text{Si}_4\text{O}_{12}$ – $\text{Mg}_3\text{Al}_2\text{Si}_3\text{O}_{12}$
469 up to 28 GPa: phase relations of garnet, ilmenite and perovskite. *Physics of the Earth and*
470 *Planetary Interiors*, 121, 85–102.
- 471 Kudoh, Y., Prewitt, C.T., Finger, L.W., Darovskikh, A., and Ito, E. (1990) Effect of iron on the
472 crystal structure of $(\text{Mg,Fe})\text{SiO}_3$ perovskite. *Geophysical Research Letters*, 17, 1481–1484.
- 473 Larson, A.C., and Von Dreele, R.B. (2004) General structure analysis system (GSAS). LANL
474 Report 86, 748.

- 475 Libowitzky, E., and Rossman, G.R. (1997) An IR absorption calibration for water in minerals.
476 American Mineralogist, 82, 1111–1115.
- 477 Libowitzky, E. (1999) Correlation of O-H stretching frequencies and O-H···O hydrogen bond
478 lengths in minerals. Hydrogen Bond Research, p. 103–115. Springer, Vienna.
- 479 Lin, J.F., Mao, Z., Yang, J., Liu, J., Xiao, Y., Chow, P., and Okuchi, T. (2016) High-spin Fe²⁺
480 and Fe³⁺ in single-crystal aluminous bridgmanite in the lower mantle. Geophysical Research
481 Letters, 43, 6952–6959.
- 482 Litasov, K., Ohtani, E., Langenhorst, F., Yurimoto, H., Kubo, T., and Kondo, T. (2003) Water
483 solubility in Mg-perovskites and water storage capacity in the lower mantle. Earth and
484 Planetary Science Letters, 211, 189–203.
- 485 Litasov, K.D., Kagi, H., Shatskiy, A., Ohtani, E., Lakshtanov, D.L., Bass, J.D., and Ito, E. (2007)
486 High hydrogen solubility in Al-rich stishovite and water transport in the lower mantle. Earth
487 and Planetary Science Letters, 262, 620–634.
- 488 Liu, Z., Fei, H., Chen, L., McCammon, C., Wang, L., Liu, R., Wang, F., Liu, B., and Katsura, T.
489 (2021) Bridgmanite is nearly dry at the top of the lower mantle. Earth and Planetary Science
490 Letters, 570, 117088.
- 491 Meade, C., Reffner, J.A., and Ito, E. (1994) Synchrotron infrared absorbance measurements of
492 hydrogen in MgSiO₃ perovskite. Science, 264, 1558–1560.
- 493 Miyagi, I., and Yurimoto, H. (1995) Water content of melt inclusions in phenocrysts using
494 secondary ion mass spectrometer. Bulletin of the Volcanological Society of Japan, 40, 349–
495 355.

- 496 Momma, K., and Izumi, F. (2011) VESTA3 for three-dimensional visualization of crystal,
497 volumetric and morphology data. *Journal of Applied Crystallography*, 44, 1272–1276.
- 498 Muir, J.M.R., and Brodholt, J.P. (2018) Water distribution in the lower mantle: Implications for
499 hydrolytic weakening. *Earth and Planetary Science Letters*, 484, 363-369.
- 500 Murakami, M., Hirose, K., Yurimoto, H., Nakashima, S., and Takafuji, N. (2002) Water in
501 Earth's lower mantle. *Science*, 295, 1885–1887.
- 502 Nakatsuka, A., Fukui, H., Kamada, S., Hirao, N., Ohkawa, M., Sugiyama, K., and Yoshino, T.
503 (2021) Incorporation mechanism of Fe and Al into bridgmanite in a subducting mid-ocean
504 ridge basalt and its crystal chemistry. *Scientific Reports*, 11, 22839.
- 505 Navrotsky, A. (1999) A lesson from ceramics. *Science* 284, 1788–1789.
- 506 Nishio-Hamane, D., Nagai, T., Fujino, K., Seto, Y., and Takafuji, N. (2005) Fe³⁺ and Al
507 solubilities in MgSiO₃ perovskite: implication of the Fe³⁺AlO₃ substitution in MgSiO₃
508 perovskite at the lower mantle condition. *Geophysical Research Letters*, 32, L16306.
- 509 Ohtani, E., Litasov, K., Hosoya, T., Kubo, T., and Kondo, T. (2004) Water transport into the
510 deep mantle and formation of a hydrous transition zone. *Physics of the Earth and Planetary*
511 *Interiors*, 143–144, 255–269.
- 512 Okuchi, T., Purevjav, N., Tomioka, N., Lin, J.-F., Kuribayashi, T., Schoneveld, L., Hwang, H.,
513 Sakamoto, N., Kawasaki, N., and Yurimoto, H. (2015) Synthesis of large and homogeneous
514 single crystals of water-bearing minerals by slow cooling at deep-mantle pressures.
515 *American Mineralogist*, 100, 1483–1492.

- 516 Panero, W.R., Pigott, J.S., Reaman, D.M., Kabbes, J.E., and Liu, Z. (2015) Dry (Mg,Fe)SiO₃
517 perovskite in the Earth's lower mantle. *Journal of Geophysical Research: Solid Earth*, 120,
518 894–908.
- 519 Pearson, D.G., Brenker, F.E., Nestola, F., McNeill, J., Nasdala, L., Hutchison, M.T., Matveev, S.,
520 Mather, K., Silversmit, G., Schmitz, S., Vekemans, B., and Vincze, L. (2014) Hydrous
521 mantle transition zone indicated by ringwoodite included within diamond. *Nature*, 507, 221–
522 224.
- 523 Portner, D.E., Rodríguez, E.E., Beck, S., Zandt, G., Scire, A., Rocha, M.P., Bianchi, M.B., Ruiz,
524 M., França, G.S., Condori, C., and Alvarado, P. (2020) Detailed structure of the subducted
525 Nazca slab into the lower mantle derived from continent-scale teleseismic P wave
526 tomography. *Journal of Geophysical Research: Solid Earth*, 125, e2019JB017884.
- 527 Prescher, C., McCammon, C., and Dubrovinsky, L. (2012) MossA: a program for analyzing
528 energy-domain Mössbauer spectra from conventional and synchrotron sources. *Journal of*
529 *applied Crystallography*, 45, 329–331.
- 530 Purevjav, N., Okuchi, T., and Hoffmann, C. (2020) Strong hydrogen bonding in a dense hydrous
531 magnesium silicate discovered by neutron Laue diffraction. *IUCrJ*, 7, 370–374.
- 532 Purevjav, N., Okuchi, T., Tomioka, N., Abe, J., and Harjo, S. (2014) Hydrogen site analysis of
533 hydrous ringwoodite in mantle transition zone by pulsed neutron diffraction. *Geophysical*
534 *Research Letters*, 6718–6724.
- 535 Purevjav, N., Okuchi, T., Tomioka, N., Wang, X., and Hoffmann, C. (2016) Quantitative
536 analysis of hydrogen sites and occupancy in deep mantle hydrous wadsleyite using single
537 crystal neutron diffraction. *Scientific Reports*, 6, 34988.

- 538 Purevjav, N., Okuchi, T., Wang, X., Hoffmann, C., and Tomioka, N. (2018) Determination of
539 hydrogen site and occupancy in hydrous Mg₂SiO₄ spinel by single-crystal neutron
540 diffraction. *Acta Crystallographica Section B*, 74, 115–120.
- 541 Ross, N.L., and Hazen, R.M. (1989) Single crystal X-ray diffraction study of MgSiO₃ perovskite
542 from 77 to 400 K. *Physics and Chemistry of Minerals*, 16, 415–420.
- 543 Sano-Furukawa, A., Hattori, T., Komatsu, K., Kagi, H., Nagai, T., Molaison, J.J., Dos Santos,
544 A.M., and Tulk, C.A. (2018) Direct observation of symmetrization of hydrogen bond in
545 delta-AlOOH under mantle conditions using neutron diffraction. *Scientific Reports*, 8,
546 15520.
- 547 Sano-Furukawa, A., Kuribayashi, T., Komatsu, K., Yagi, T., and Ohtani, E. (2011) Investigation
548 of hydrogen sites of wadsleyite: A neutron diffraction study. *Physics of the Earth and
549 Planetary Interiors*, 189, 56–62.
- 550 Schultz, A.J., Jørgensen, M.R.V., Wang, X.P., Mikkelsen, R.L., Mikkelsen, D.J., Lynch, V.E.,
551 Peterson, P.F., Green, M.L., and Hoffmann, C.M. (2014) Integration of neutron time-of-
552 flight single-crystal Bragg peaks in reciprocal space. *Journal of Applied Crystallography*, 47,
553 915–921.
- 554 Shimizu, K., Ushikubo, T., Hamada, M., Itoh, S., Higashi, Y., Takahashi, E., and Ito, M. (2017)
555 H₂O, CO₂, F, S, Cl, and P₂O₅ analyses of silicate glasses using SIMS: Report of volatile
556 standard glasses. *Geochemical Journal*, 51, 299–313.
- 557 Spektor, K., Nylen, J., Mathew, R., Edén, M., Stoyanov, E., Navrotsky, A., Leinenweber, K., and
558 Häussermann, U. (2016) Formation of hydrous stishovite from coesite in high-pressure
559 hydrothermal environments. *American Mineralogist*, 101, 2514–2524.

- 560 Sugahara, M., Yoshiasa, A., Komatsu, Y., Yamanaka, T., Bolfan-Casanova, N., Nakatsuka, A.,
561 Sasaki, S., and Tanaka, M. (2006) Reinvestigation of the MgSiO₃ perovskite structure at
562 high pressure. *American Mineralogist*, 91, 533–536.
- 563 Suzuki, A., Ohtani, E., Kondo, T., and Kuribayashi, T. (2001) Neutron diffraction study of
564 hydrous phase G: Hydrogen in the lower mantle hydrous silicate, phase G. *Geophysical*
565 *Research Letters*, 28, 3987–3990.
- 566 Thompson, A.B. (1992) Water in the Earth's upper mantle. *Nature*, 358, 295–302.
- 567 Tomioka, N., Okuchi, T., Purevjav, N., Abe, J., and Harjo, S. (2016) Hydrogen sites in the dense
568 hydrous magnesian silicate phase E: a pulsed neutron powder diffraction study. *Physics and*
569 *Chemistry of Minerals*, 43, 267–275.
- 570 Townsend, J.P., Tsuchiya, J., Bina, C.R., and Jacobsen, S.D. (2016) Water partitioning between
571 bridgmanite and postperovskite in the lowermost mantle. *Earth and Planetary Science*
572 *Letters*, 454, 20–27.
- 573 Trots, D.M., Kurnosov, A., Manthilake, M.A.G.M., Ovsyannikov, S.V., Akselrud, L.G., Hansen,
574 T., Smyth, J.R., and Frost, D.J. (2013) The determination of hydrogen positions in
575 superhydrous phase B. *American Mineralogist*, 98, 1688–1692.
- 576 Zikovsky, J., Peterson, P.F., Wang, X.P., Frost, M.J., and Hoffmann, C. (2011) CrystalPlan: an
577 experiment-planning tool for crystallography. *Journal of Applied Crystallography*, 44, 418–
578 423.
- 579

580 **Figure and Table captions**

581

582 Table 1. Major-element composition of two representative bridgmanite crystals analysed by
583 EPMA. The weight percent of each oxide component is listed, where FeO* is determined
584 assuming all Fe is Fe²⁺. Total average# values of the two crystals were used for the neutron
585 structure refinement.

586

587 Table 2. Refined structure parameters of the (Fe, Al)-bearing bridgmanite. Initial atomic
588 coordinates in the refinements were taken from Horiuchi et al. (1987). See the text for the
589 refinement procedure in detail.

590

591 Figure 1. The crystal structure of (Fe, Al)-bearing bridgmanite with an orthorhombic symmetry
592 (space group *Pbnm*). The bridgmanite structure consists of A site cations, B site cations, and
593 oxygen anions with an ABO₃ perovskite-type framework. In the illustration, the A sites are
594 visible as brown spheres while the B sites are hidden inside blue-colored BO₆ octahedra. The
595 illustration was produced using VESTA3 (Momma and Izumi, 2011).

596

597 Figure 2. Synthesis and characterizations of the (Fe, Al)-bearing bridgmanite crystals. All scale
598 bars shown with black color are 100 μm in length. (a) A stereo microscope image of the
599 recovered bridgmanite crystals with dark-brownish color and subhedral to euhedral forms. (b) A
600 micro-focused X-ray diffraction pattern of the recovered aggregates with a mixture of the
601 bridgmanite (asterisks), brucite (Br), and DHMS phase D (D), respectively, indicating that the
602 bridgmanite crystals were grown under nearly water-saturated condition. The inset shows the

603 appearance of the aggregates. (c) Double-side polished crystal of the (Fe, Al)-bearing
604 bridgmanite with a thickness of ~ 200 μm . The red circles indicate the areas for Mössbauer
605 measurements. (d) Mössbauer spectrum of the bridgmanite crystal. The spectrum was collected
606 using a ^{57}Co point source with a beam size of 300 μm and a collection time of ~ 40 hours. The
607 spectrum was fit with two doublets, corresponding to Fe^{2+} (green) and Fe^{3+} (blue) using the
608 MossA program (Prescher et al., 2012). Analysis of the spectrum shows ~ 52 % $\text{Fe}^{3+}/\Sigma\text{Fe}$ and
609 ~ 48 % $\text{Fe}^{2+}/\Sigma\text{Fe}$.

610

611 Figure 3. TEM/STEM micrographs of the (Fe, Al)-bearing bridgmanite crystal. (a) A bright-field
612 TEM image of a representative thin foil which shows homogeneous crystal without visible
613 inclusions or defects. (b) A bright-field STEM image showing the lattice fringes of (001). (c) A
614 Fourier-noise-filtered image of (b) which confirmed high-quality lattice spaces without
615 disturbances. (d) A selected-area electron diffraction (SAED) pattern along the $[1-10]$ zone axis
616 for a selected area of the crystal. The SAED pattern shows sharp reflection spots of the
617 bridgmanite structure.

618

619 Figure 4. Polarized infrared absorption spectra, pole figures, and photographs of the oriented
620 crystal sections of bridgmanite. (a) A series of spectra measured from the section cut normal to
621 the a -axis and double-side polished into $350(\pm 10)$ μm thickness. It was measured along the
622 orientation from 0° (the polarization of the IR beam parallel to the c -axis) via 90° (parallel to the
623 b -axis) to 180° (again parallel to the c -axis). (b) A series of spectra measured from the section cut
624 normal to the c -axis and double-side polished into $100(\pm 10)$ μm thickness. It was measured along

625 the orientation from 0° (the polarization of the IR beam parallel to the *a*-axis) via 90° (parallel to
626 the *b*-axis) to 180° (again parallel to the *a*-axis).

627 (c, d) The couple of pole figures corresponding to the series of spectra (a) and (b). These show
628 intensity trend of integrated absorbances of 3480 cm⁻¹ (open circle) and 3160 cm⁻¹ (filled circle)
629 bands, respectively. (e, f) The measured crystal sections cut normal to the *a* and *c* axes,
630 respectively.

631 For each spectrum shown in (a) and (b), a baseline for the window of O-H stretching region (2300
632 to 3800 cm⁻¹) was defined as a spline function covering the original spectrum from 1500 to 4000
633 cm⁻¹, and was subtracted from the original. This baseline was close to linear in the window of the
634 O-H stretching region. For defining each point shown in (c) and (d), a nonlinear peak-fitting
635 analysis was conducted to resolve overlapped Gaussian peaks within the series of spectra (a) and
636 (b).

637

638 Figure 5. Results of hydrogen concentration analysis for the bridgmanite (Bdg) crystals by SIMS.
639 The solid and broken lines show correlations between ¹H/³⁰Si count ratios and water
640 concentrations using natural amphibole (Amp) and basaltic glass (EPR-3G) as the standards,
641 respectively. San Carlos olivine (SC) was used as the dry reference standard. Two independent
642 H₂O concentrations from the two crystals (an enlarged region is shown in the inset) were
643 obtained using the averages of all data points from each crystal.

644

645 Figure 6. A difference-Fourier map sectioned normal to the *c*-axis of the bridgmanite. The map
646 shows residual nuclear density distribution after removing scattering contributions from all major
647 cations and anions other than hydrogen. The A sites (shown in brown color) are occupied by Mg,

648 Fe, and Al cations, whereas the B sites (shown in gray color) are occupied by Al and Si cations.
649 This map simultaneously shows positive (blue color) and negative (yellow and red colors)
650 residuals of the scattering density. We evaluated each of the apparent negative residual in the
651 three-dimensional map volume, including those not shown in this section, for finding the
652 possible hydrogen site position (see the text for details). After the evaluation, a negative residual
653 of $-1.16 \text{ fm}/\text{\AA}^3$, as highlighted by the black-dashed circle, was determined as the primary
654 hydrogen site position. The hydrogen is located between two O1 oxygen anions, with OH
655 covalent bonding direction close to the *b* axis.

656

657 Figure 7. The refined hydrogen site occupancies as a function of the resolution in space. The
658 hydrogen site was refined as $(x, y, z = 0.288, 0.143, 0.25)$ (see Table 2). These occupancies were
659 determined one by one for a series of reflection intensity datasets with different minimum *d*-
660 spacings from 0.40 Å to 0.60 Å.

Crystal Point	1					2					1 and 2
	1	2	3	4	average	1	2	3	4	average	average [#]
SiO ₂	51.6	51.5	52.0	51.9	51.8(2)	49.4	51.2	51.3	50.9	50.7(9)	51.2(8)
Al ₂ O ₃	7.1	7.5	7.1	6.9	7.1(3)	6.8	7.5	7.6	7.5	7.4(4)	7.2(3)
MgO	34.7	34.5	34.6	34.7	34.6(1)	33.6	34.6	34.4	34.3	34.2(5)	34.4(4)
FeO*	6.6	6.8	6.5	6.5	6.6(1)	8.9	7.1	7.2	7.1	7.6(9)	7.1(8)
Total	100.0	100.3	100.2	99.9	100.1(2)	98.6	100.5	100.5	99.7	99.8(9)	100.0(6)

Table 1

Wyckoff positions	Atoms	Coordinates			Occupancies	Debye-Waller factors ($\times 10^3$, Å^2)						
		x	y	z		U ₁₁	U ₂₂	U ₃₃	U ₁₂	U ₁₃	U ₂₃	U _{iso}
4b (A-site)	Mg				0.877							0
	Fe	0.51446(7)	0.55654(5)	0.25	0.101	0.370(10)	0.352(7)	0.601(8)	0.080(7)	0		
	Al				0.034(1)							
4b (B-site)	Si				0.875							
	Al	0.5	0	0	0.113(1)	0.150(10)	0.143(8)	0.174(8)	0	0	0.013(6)	
4c	O1	0.10543(5)	0.46321(4)	0.25	0.998(1)	0.346(8)	0.356(6)	0.320(6)	0	0	0	
8d	O2	0.19497(4)	0.20015(3)	0.55449(2)	1.000(1)	0.365(6)	0.372(4)	0.419(5)	0.070(4)	0.069(4)	0.084(4)	
4c	H	0.288(14)	0.143(13)	0.25	0.010(3)							3(1)

Table 2

y

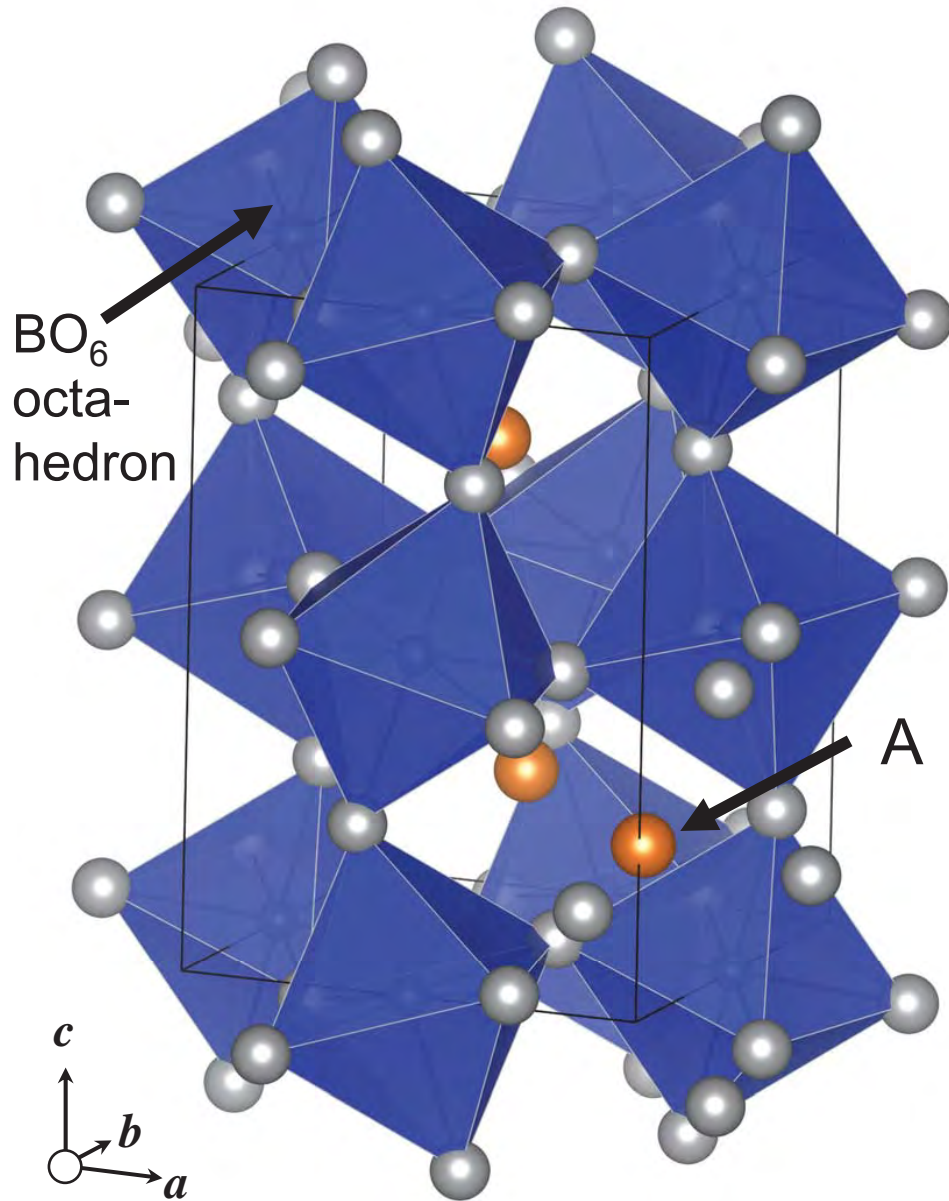


Figure 1

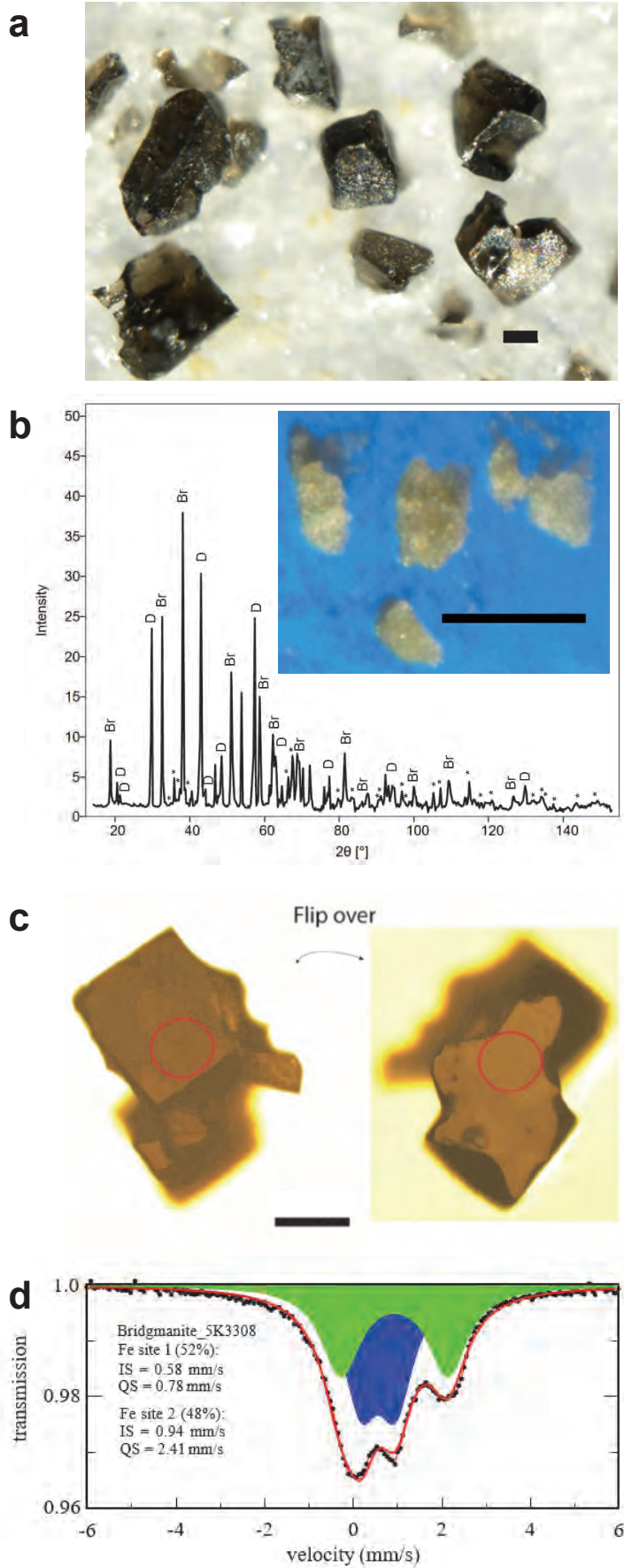


Figure 2

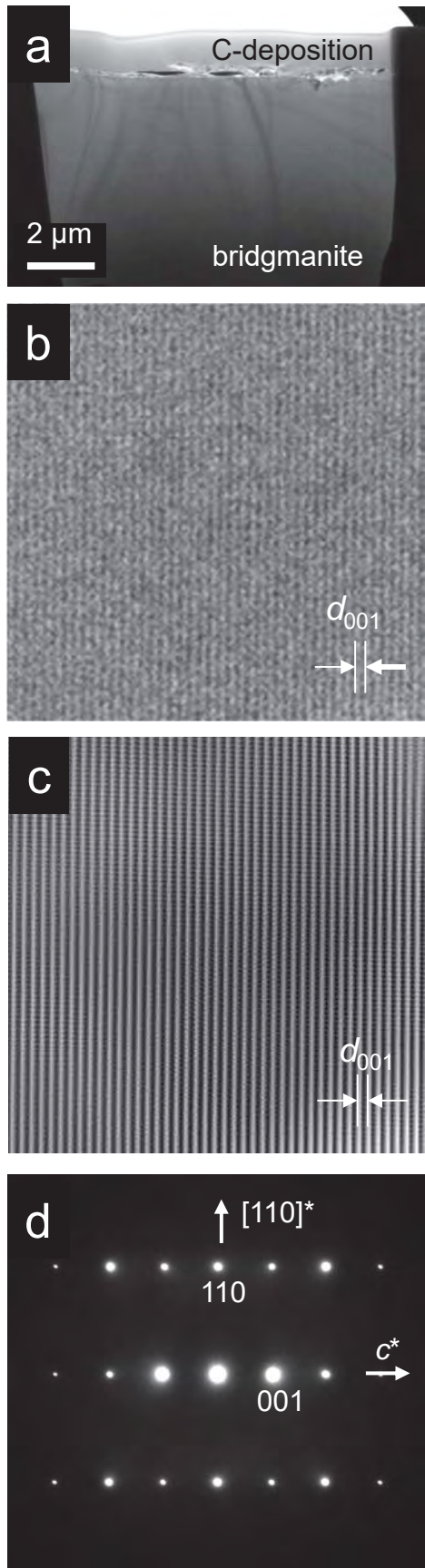


Figure 3

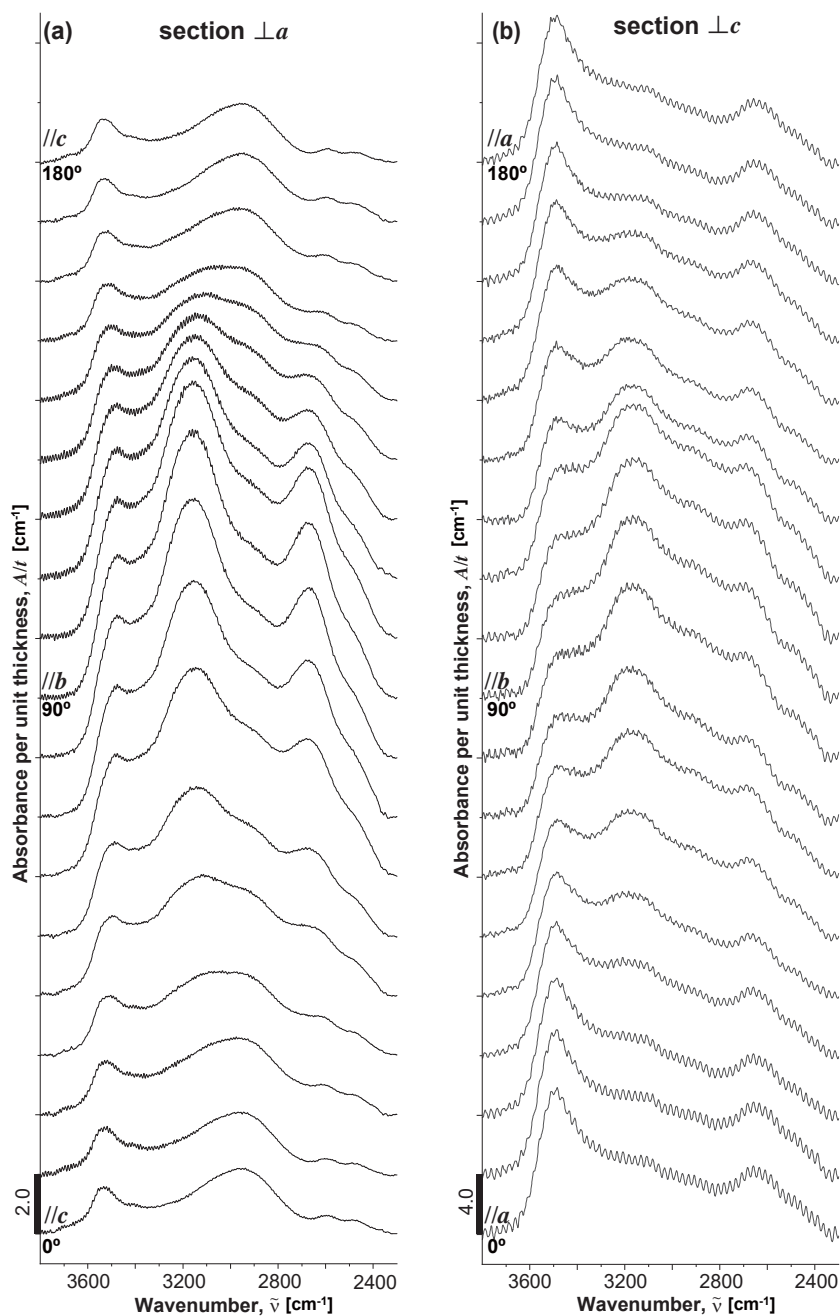
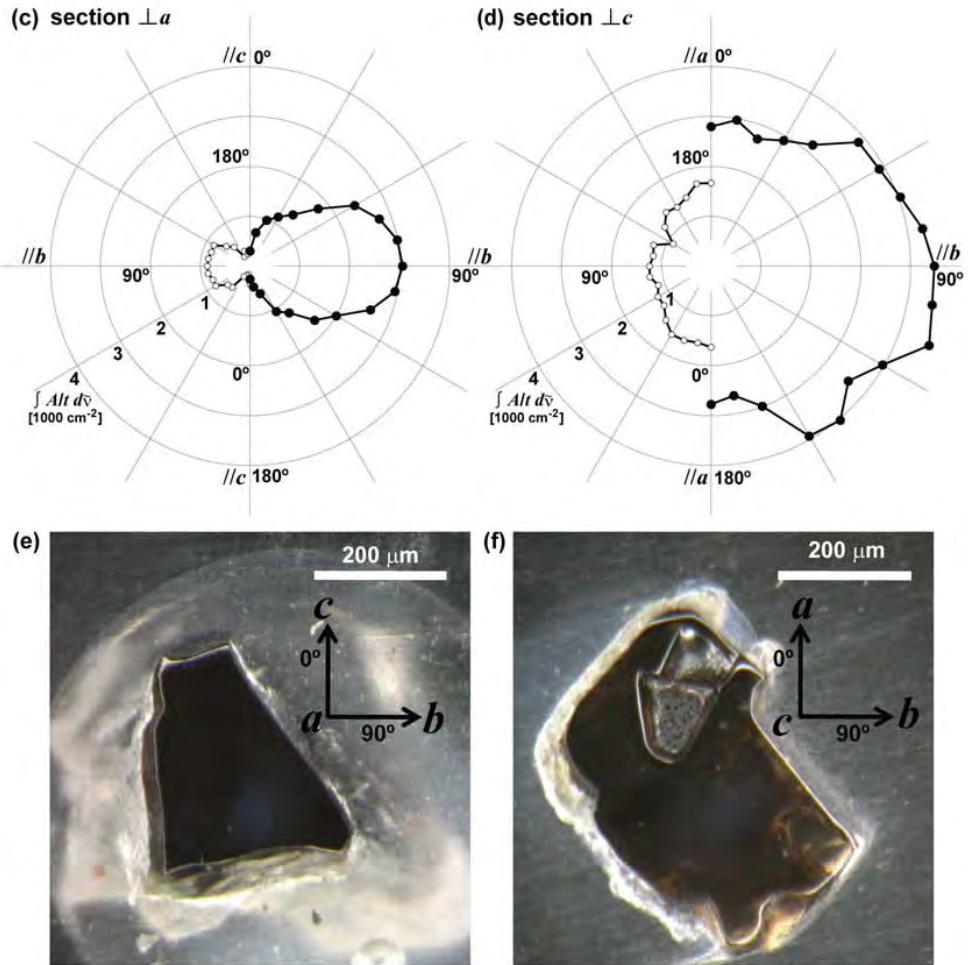


Figure 4



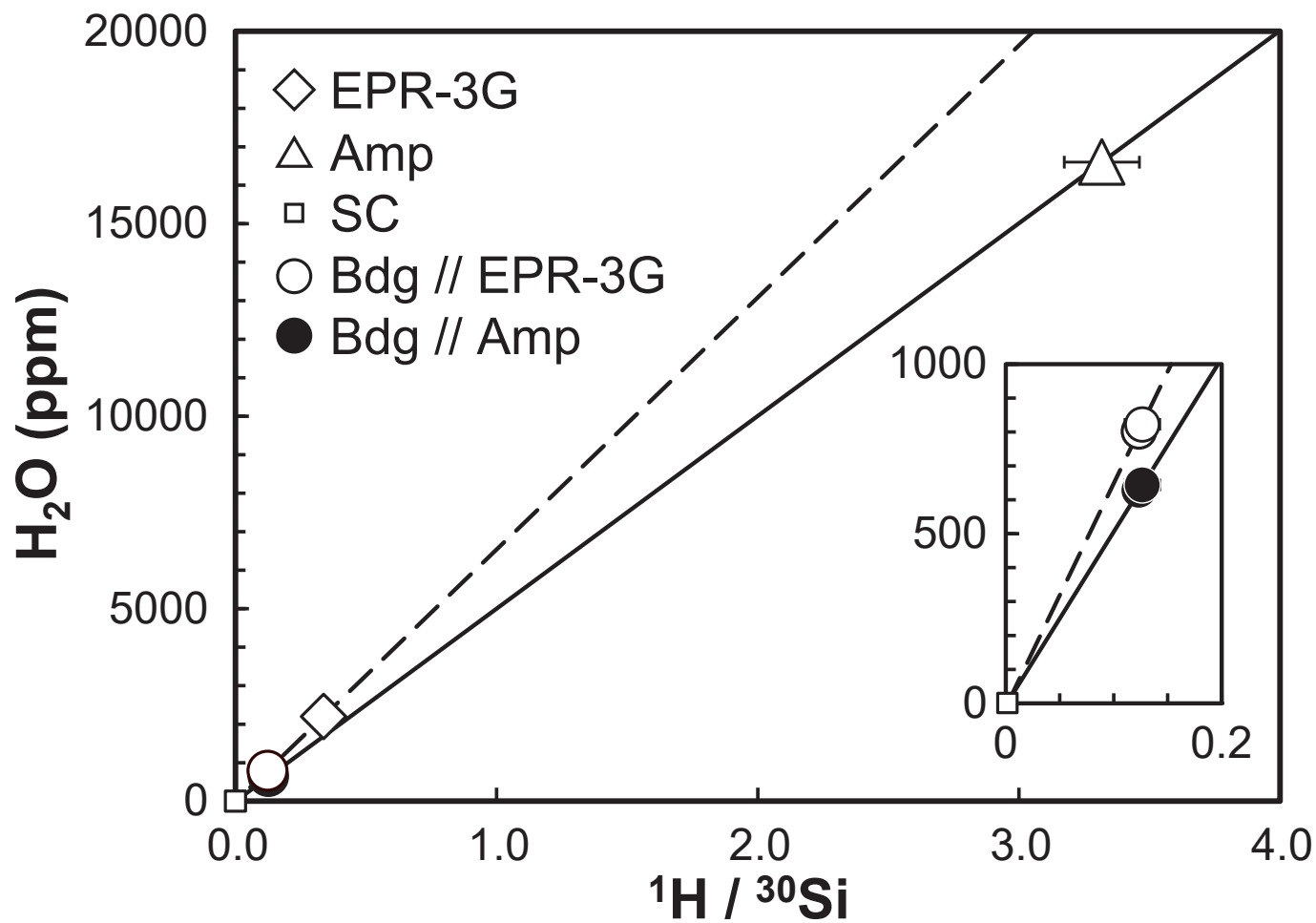


Figure 5

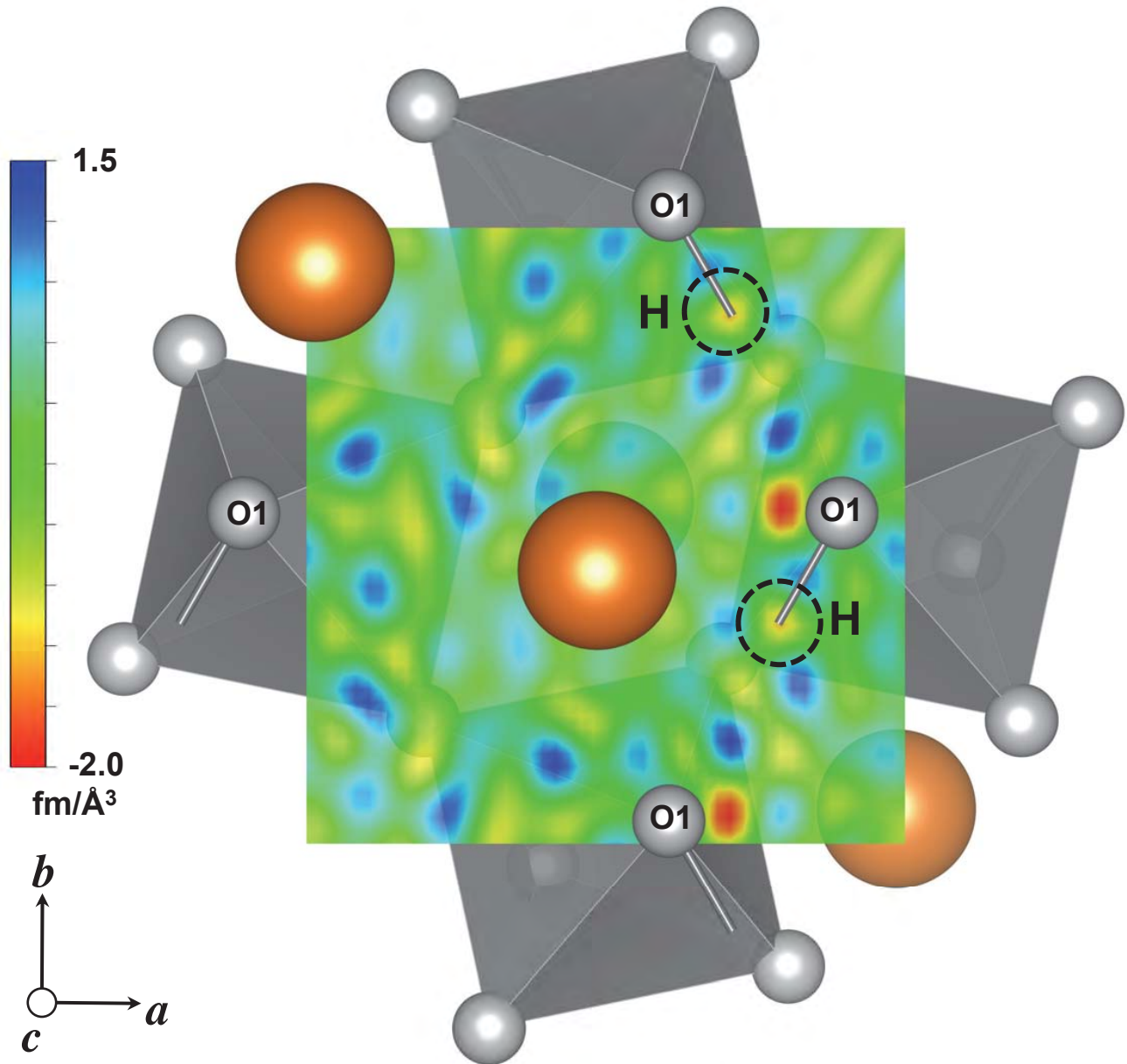


Figure 6

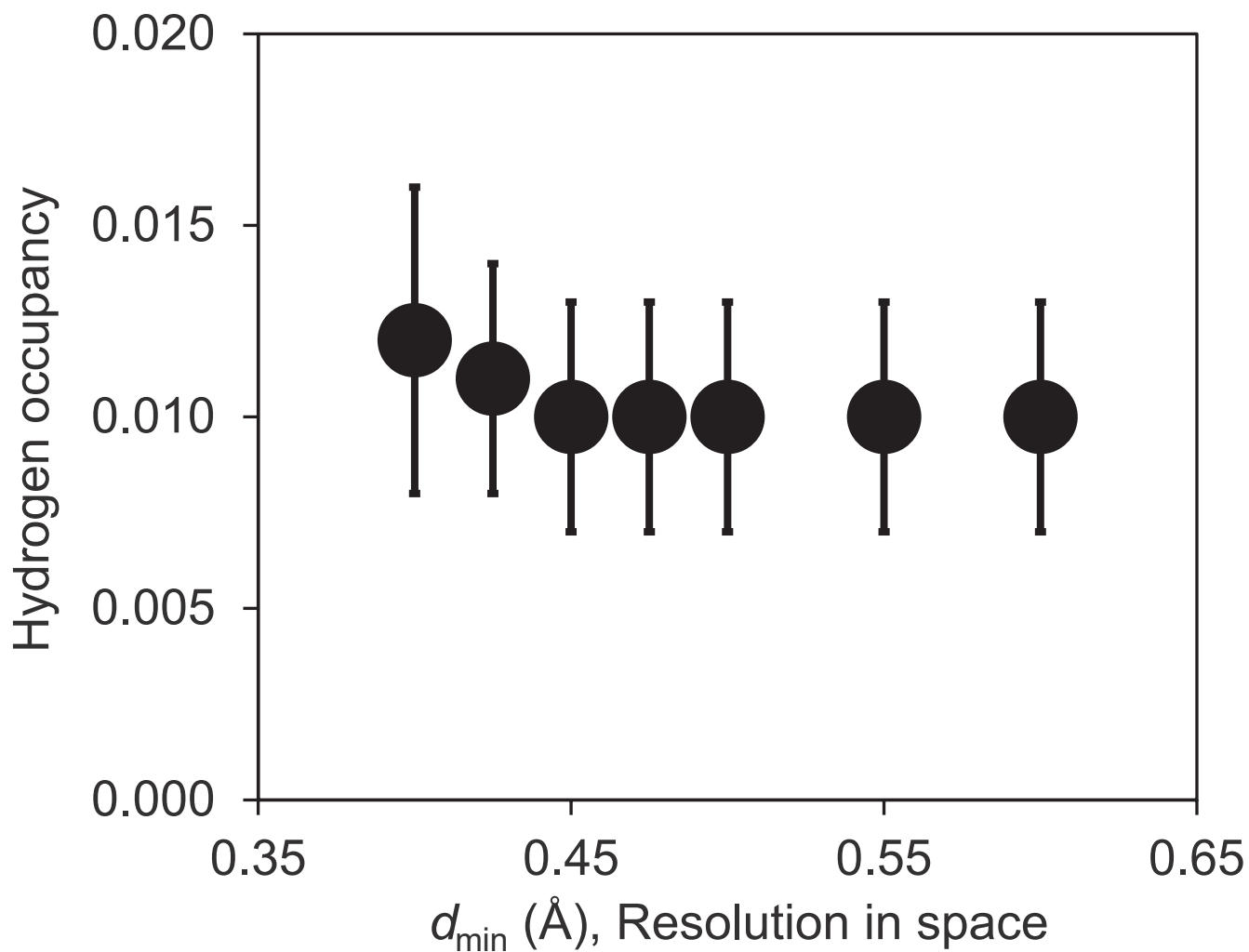


Figure 7